



Charge separation between wurtzite ZnO polar {001} surfaces and their enhanced photocatalytic activity



Yan Chen^{a,b}, Hua Zhao^a, Bin Liu^a, Heqing Yang^{a,*}

^a Key Laboratory of Macromolecular Science of Shaanxi Province, School of Materials Science and Engineering, Shaanxi Normal University, Xi'an 710062, China

^b School of Chemistry and Chemical Engineering, Xianyang Normal University, Xianyang 712000, China

ARTICLE INFO

Article history:

Received 30 May 2014

Received in revised form 17 July 2014

Accepted 21 July 2014

Available online 28 July 2014

Keywords:

ZnO

Photocatalytic activity

Polar {001} surfaces

A charge separation model

ABSTRACT

ZnO nanocrystals with various (002) orientations were synthesized via a solvothermal reaction of zinc acetate with n-butylamine (BA) and tetrahydrofuran at 140 °C for 12 h by varying the molar ratio of BA to Zn(II). The formation of the ZnO nanocrystals with various (002) orientations and shapes results from the selective adsorption of different amount of BA molecules on ZnO (001) surface. Photocatalytic activity of the as-prepared ZnO nanocrystals with various (002) orientations in degradation of methyl orange was studied, it was found that the exposed {001} facets are reactive facets. The structure and atomic charge distribution of the {001} facets were studied by periodic density functional theory calculations. Based on polar structure of the exposed {001} surfaces, a charge separation model between polar ZnO {001} surfaces was proposed. There is an internal electric field between positive Zn–ZnO (001) and negative O–ZnO (00 $\bar{1}$) planes due to the spontaneous polarization. The internal electric field provides the driving force for charge separation. The reduction and oxidation reactions take place on the positive (001) and negative (00 $\bar{1}$) polar planes, respectively. The charge separation model can deepen understanding of charge transfer in the semiconductor nanocrystal with highly photocatalytic activities and offer guidance to design more effective photocatalysts as well as new type solar cells, photoelectrodes or photoelectric devices.

© 2014 Elsevier B.V. All rights reserved.

1. Introduction

The physical and chemical properties of semiconductor nanocrystals are not only sensitive to crystal size but also to crystal shape. Thus, shape-controlled synthesis of semiconductor nanocrystals has attracted increasing research interest [1–3]. Zinc oxide, a direct wide-band-gap semiconductor with a band gap of 3.37 eV and a large exciton binding energy (60 meV) [4], is an important functional material. It has been studied widely due to its unique optoelectronic property, chemical and thermal stability and promising applications for UV lasers [5], field-effect transistors [6], photodetectors [7], gas sensors [8], solar cells [9] and piezoelectric generators [10].

On the other hand, ZnO is still one of the most important semiconductor photocatalysts [11–27]. In this regard, Li et al. [11] investigated photocatalytic activity of spherical particles, ellipsoidal aggregates, rod-like particles, needle aggregates, single

crystallite particles and irregular particles of ZnO for decomposition of acetaldehyde, and found that the particle morphology significantly affects its photocatalysis. Jang et al. [12] studied photocatalytic activity for H₂O₂ generation of nanorods, nanoplates, microrods, dumbbell-shaped microrods of ZnO and demonstrated that fine-tuning of face orientation results in optimization of the photocatalytic activity. Subsequently, it was reported that nanorods with a cone and small aspect ratio [13], tetrapods [14], nanorod arrays [15], flower-like structures assembled from nanorods [16], nanotube arrays [17], nanobelt arrays [18], nanodisks [19], nanoplatelets as thin as 10 nm [20], nanosheet networks grown on the hexagonal-pyramid microcrystals [21], porous nanobelts [22], microspheres assembled from porous nanosheets [23], porous nanosheets grown on a nanorod [24], flowerlike structures assembled from nanosheets [25], nanoporous networks [26] and porous spheres [27] of ZnO exhibited enhanced photocatalytic activity. However, increasing reason of the photocatalytic activity is not yet clear. In addition, controllable synthesis of ZnO nanocrystals with various (002) orientations and their (002) orientation dependent photocatalytic activity have never been reported until now.

* Corresponding author. Fax: +86 29 81530702.
E-mail address: hqyang@snnu.edu.cn (H. Yang).

Recently, crystal facet engineering of semiconductors is found to be an effective strategy to increase photocatalytic performances. The anatase TiO_2 [28] and hexagonal CdS [29,30] $\{001\}$ facets as well as cubic Cu_2O $\{111\}$ facets [31] have been found to be highly reactivity facets. However, the mechanism involved in the photocatalysis is not yet known.

Herein, we report on the controllable growth of ZnO nanocrystals with various (002) orientations in the zinc acetate-*n*-butylamine (BA)-tetrahydrofuran (THF) solvothermal systems by varying the molar ratio of BA to Zn(II). Photocatalytic activity of the as-obtained ZnO nanocrystals with various (002) orientations in degradation of methyl orange (MO) were investigated, it was found that the exposed $\{001\}$ facets are highly reactive facets. Structure and atomic charge distribution of the $\{001\}$ facets were studied by periodic density functional theory (DFT) calculations. Based on polar structure of the exposed $\{001\}$ surfaces, a charge separation model between polar $\{001\}$ surfaces was proposed to explain the enhanced photocatalytic activities.

2. Experimental

2.1. Preparation

Zinc acetate was from the Xi'an chemical reagent factory, China. THF and BA were from the Sinopharm Chemical reagent Co., Ltd. All reagents used were of analytical purity and were directly used without further purification. In a typical procedure, 0.250 g (1.1 mmol) of zinc acetate and 10.5 mL of a mixture of BA and THF were put into a beaker of 50 mL capacity. The mixture was stirred for 10 min to form a clear solution. The solution was transferred into a Teflon-lined stainless steel autoclave of 50 mL capacity. The autoclave was sealed and heated at 140°C for 12 h. After the heating treatment, the autoclave was cooled to room temperature naturally. The products were collected by centrifugation, washed three times with deionized water and ethanol, respectively, and finally dried in air for further characterization.

2.2. Characterization

The as-prepared products were characterized and analyzed using X-ray diffraction (XRD), scanning electron microscopy (SEM), transmission electron microscopy (TEM) and infrared (IR) spectroscopy. The XRD analysis was performed using a Rigaku D/MAX-IIIC X-ray diffractometer with $\text{Cu K}\alpha_1$ radiation ($\lambda = 1.54056 \text{ \AA}$) at 40 kV and 30 mA. The scanning speed was $8^\circ/\text{min}$. SEM images were obtained using a FEI Quanta 200 scanning electron microscope at an accelerating voltage of 20 kV. TEM and electron diffraction images were obtained using a JEOL JEM-3010 transmission electron microscope at an accelerating voltage of 300 kV. Samples for TEM were prepared by dispersing powders on a carbon-coated copper grid. The IR spectrum was recorded using a Bruker Equinox 55 fourier transform IR spectrophotometer at room temperature. The Brunauer-Emmett-Teller (BET) specific surface area determination was performed by N_2 gas adsorption using an America Micromeritics ASAP 2020 surface analytical instrument.

The Structures and atomic charges of the wurtzite ZnO $\{001\}$ facets were calculated by using the DMOL3 code [32] and the generalized gradient approximation (GGA) with Perdew-Burke-Ernzerhof (PBE) functional is employed as the exchange-correlation functional theory [33]. The atomic charges are computed using Hirshfeld [34] population analyses.

2.3. Evaluation of photocatalytic activity

Photocatalytic property of the ZnO in various geometrical morphologies was examined by measuring the decoloration of MO

aqueous solution. 20.0 mg of the as-prepared products and 20.0 mL of $5 \times 10^{-5} \text{ mol/L}$ MO solution ($\text{pH}=6.0$) were added to a 50 mL of quartz test tube. The suspension was magnetically stirred for 10 min to establish a adsorption/desorption equilibrium between the dye and the ZnO catalysts. The mixed solution was then irradiated with a 300 W Hg lamp at a distance of about 8 cm (XPA-7 photochemical reactor, Xujiang Electromechanical Plant, Nanjing, China). At a given irradiation time interval, 3 mL of samples were withdrawn from the test tube for analysis. Sample solutions were obtained by centrifugation, and their absorption spectra were measured by on a U-2910 ultraviolet-visible spectrophotometer (Hitachi High-Technologies Corporation, Tokyo, Japan) using deionized water as a reference. For comparison, the photocatalytic activity of commercial TiO_2 (Degussa P25) was also tested under the same reaction conditions and with the equal catalyst weight to that employed for ZnO.

3. Results and discussion

3.1. Morphology and crystal structure

The products prepared by varying molar ratio of BA to Zn(II) in the zinc acetate-BA-THF solvothermal system were characterized by SEM and XRD. Fig. 1a shows the SEM images of the products obtained in the solvothermal system with the molar ratio of 5/1.1. It is clearly observed that the products consist of a quantity of cone-shaped structures. The base diameters and heights of the cone-shaped crystals are in the range of 200–400 and 350–700 nm, respectively. When the molar ratio of BA to Zn(II) is increased to 10/1.1, the as-synthesized products consist of platform-shaped structures with thickness of about 270 nm (Fig. 1b). The platform-shaped structures have a flat hexagonal crystallographic plane, and the side lengths and diagonals of top hexagonal faces are 190–230 and 370–430 nm, respectively. Those of the bottom hexagonal faces are 290–350 and 570–670 nm, respectively. When the molar ratio of BA to Zn(II) increased to 15/1.1 or 45/1.1, the as-synthesized products consist of hexagonal disk shaped structures (Fig. 1c and d). The side length, diagonal and thickness of the hexagonal nanodisks obtained at molar ratio of 15/1.1 are 270–310, 500–660 and about 150 nm, respectively. As the molar ratio of BA to Zn(II) is 45/1.1, the side length and diagonal of the hexagonal nanodisks increase to 0.8–1.2 and 1.8–2.4 μm , respectively, and the thickness decreases to 60–100 nm. These results suggest that controllable synthesis of ZnO nanocrystals with various shapes can be achieved by varying the molar ratio of BA to Zn(II). The as-obtained ZnO nanocrystals synthesized at the molar ratio of BA to Zn(II) of 5/1.1, 10/1.1, 15/1.1, 45/1.1 are denoted as sample 1, 2, 3 and 4, respectively, and are listed in Table 1.

Fig. 2a shows the XRD patterns of the as-obtained ZnO nanocrystals with various shapes by adjusting the molar ratio of BA to Zn(II). All diffraction peaks can be attributed to ZnO phase with a hexagonal structure (Joint Committee on Powder Diffraction Standards (JCPDS) card No. 36-1451). No peaks of other impurities can be detected, which indicates that the as-obtained ZnO nanocrystals with various shapes are pure wurtzite ZnO. Moreover, the (002) intensity increases with an increase on the molar ratio of BA to Zn(II), indicating (002) face orientation is enhanced. The texture coefficient of (002) plane ($\text{TC}_{(002)}$) is defined as [35]

$$\text{TC}_{(002)} = \frac{I_{(002)}}{I_{(002)}^0} \left\{ \frac{1}{n} \sum I_{hkl}^0 \right\}^{-1} \quad (1)$$

where $I_{(hkl)}$ are measured intensities of (hkl) reflection, I_{hkl}^0 are powder diffraction intensities of wurtzite ZnO according to the JCPDS card no. 36-1451, and n is the number of diffraction peaks

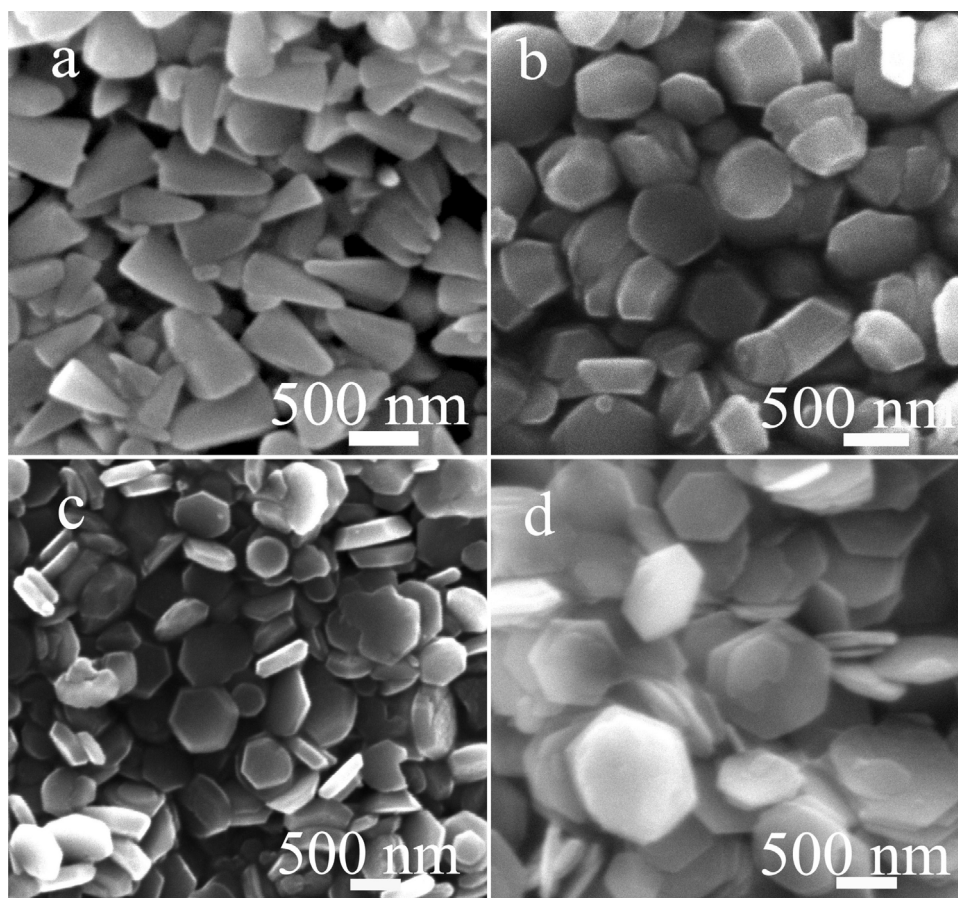


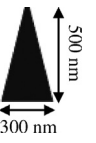
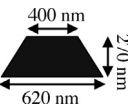
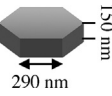
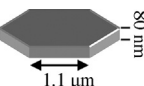
Fig. 1. SEM images of the products prepared in the solvothermal system with the molar ratio of BA to Zn(II) of (a) 5/1.1, (b) 10/1.1, (c) 15/1.1 and (d) 45/1.1.

used in the calculations. For materials with random crystallographic orientations, e.g. powders, the texture coefficient is 1. Values of $TC_{(002)}$ for the as-synthesized samples 1, 2, 3 and 4 are 0.80, 1.20, 1.56 and 2.51, respectively (Table 1). The $TC_{(002)}$ value increases with an increase in the molar ratio of BA/Zn(II), as shown in Fig. 2b.

Further morphological and structural characterization of the as-synthesized hexagonal cone and disk shaped structures (samples 1 and 3) investigated by TEM. Fig. 3a shows a typical TEM image of the hexagonal ZnO nanocones (sample 1). The length of the ZnO nanocone is about 500 nm, which is consistent with the SEM results. The selected-area electron diffraction (SAED) pattern from

Table 1

$TC_{(002)}$, percentage of $\{001\}$ surfaces, BET, K and k' of ZnO nanocrystals with various shapes obtained by varying the molar ratio of BA to Zn(II).

	Volume of THF (mL)	Volume of BA (mL)	Molar ratio of BA/Zn(II)	Shape	$TC_{(002)}$	Percentage of $\{001\}$ surfaces (%)	BET ($m^2 g^{-1}$)	K (min^{-1})	k' ($min^{-1} m^2$)
Sample 1	10.0	0.5	5/1.1		0.80	–	2.62	0.0071 ± 0.0002	0.135
Sample 2	9.5	1.0	10/1.1		1.20	–	2.68	0.0093 ± 0.0003	0.174
Sample 3	9.0	1.5	15/1.1		1.56	62.0	2.74	0.0109 ± 0.0004	0.199
Sample 4	6.0	4.5	45/1.1		2.51	92.0	2.25	0.0256 ± 0.0008	0.569
P25	–	–	–	–	–	–	50.07	0.0376 ± 0.0022	0.038

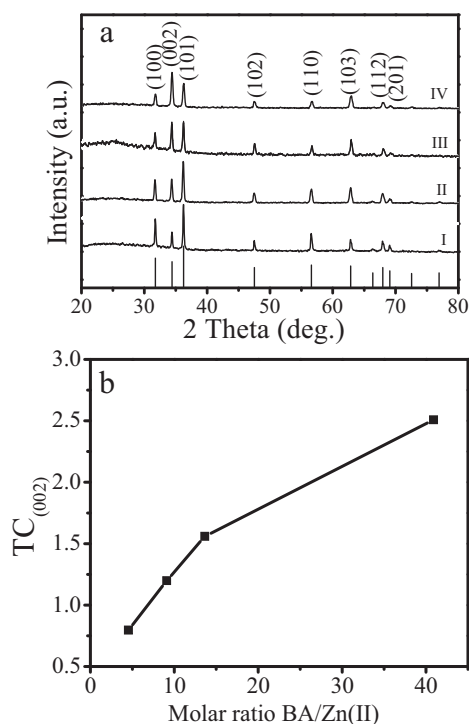


Fig. 2. (a) XRD patterns of the products prepared in the solvothermal system with the molar ratio of BA to Zn(II) of (I) 5/1.1, (II) 10/1.1, (III) 15/1.1 and (IV) 45/1.1. The stick pattern is the standard XRD pattern for ZnO powders (JPCDS card file no.36-1451). (b) The $TC_{(002)}$ value of the as-obtained ZnO nanocrystals with different shapes as a function of BA/Zn(II) ratio.

box in (a) is shown in Fig. 3b, which can be indexed as the $[2\bar{1}0]$ zone axis of ZnO with the hexagonal structure. The corresponding high resolution TEM (HRTEM) image is shown in Fig. 3c. The lattice spacing of 0.52 nm can be observed clearly from the HRTEM image, which corresponds to (001) facets. Both the SAED and the HRTEM confirm that the hexagonal ZnO nanocones are single crystalline and grow along the $[001]$ direction. Fig. 4a shows a typical TEM image of hexagonal ZnO nanodisks (sample 3). The nanodisk has perfect hexagonal shape with a side length of about 310 nm and a diagonal of about 620 nm. The SAED pattern from box in (a) is shown in Fig. 4b, which can be indexed as the $[001]$ zone axis of ZnO with the hexagonal structure. The corresponding HRTEM image is displayed in Fig. 4c. The spacing of the crystallographic planes measured from the HRTEM image is about 0.28 nm, corresponding to the distance between (100) crystal planes. The SAED and HRTEM results indicate that the nanodisks grow mainly along six symmetric directions of $\pm[100]$, $\pm[1\bar{1}0]$, and $\pm[010]$, and are enclosed by $\pm(001)$ top and bottom surfaces. Percentage of {001} surfaces of samples 3 and 4 is measured, and the results are shown in Table 1.

3.2. Formation mechanism of ZnO nanocrystals with different shapes

In order to understand the role of BA in the formation of ZnO nanocrystals with different shapes, the products prepared in the zinc acetate-THF solvothermal system without BA were characterized by SEM and XRD, and the results are shown in Fig. 5a and b. The SEM observation shows the as-obtained products consist of a large quantity of nanoparticles with unregular shapes. The XRD pattern indicates that the nanoparticles with unregular shapes are pure wurtzite ZnO. It is reasonable to conclude that BA plays a vital role in the formation of these ZnO nanocrystals with different shapes. In addition, the as-synthesized ZnO nanodisks (sample

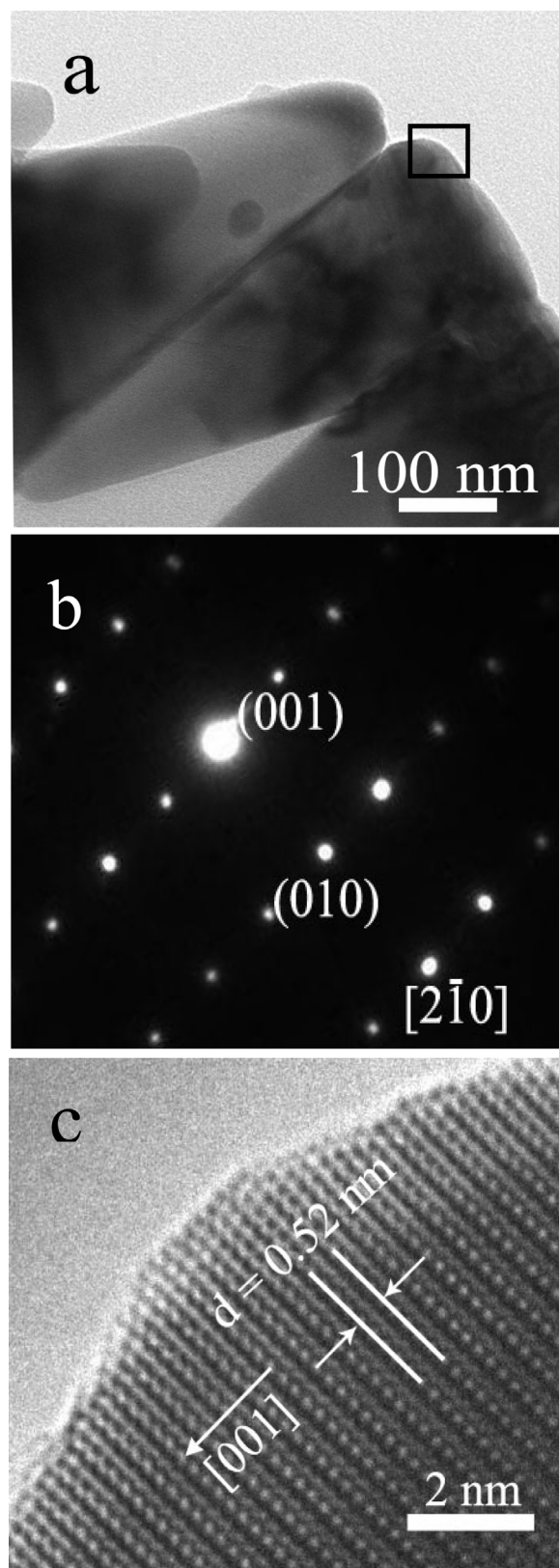


Fig. 3. (a) TEM image of the ZnO nanocones (sample 1), (b) SAED pattern and (c) HRTEM image from box in (a).

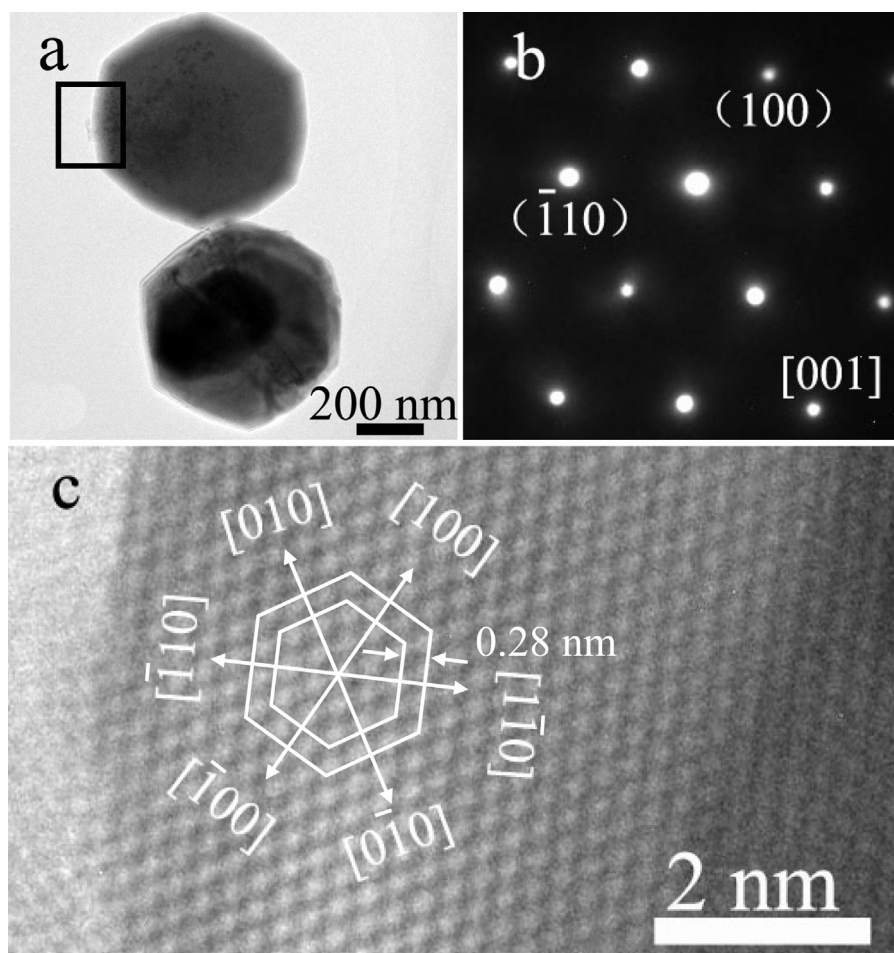
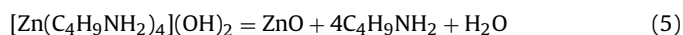
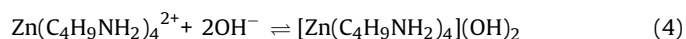
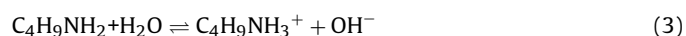
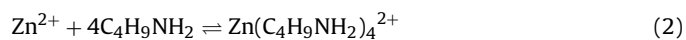


Fig. 4. (a) TEM image of the ZnO nanodisks (sample 3), (b) SAED pattern and (c) HRTEM image from box in (a).

3) were examined by using IR spectroscopy, and the result is shown in Fig. 5c. In the IR spectrum, the wide and strong absorption band at about 3442 cm^{-1} , which corresponds to O–H stretching vibration, could be due to the absorption of H_2O in the sample [36]. The absorption in this range, however, overlaps with that of NH_2 asymmetric and symmetric stretching vibrations, which makes it difficult to identify NH_2 group of BA [36]. The bands at 1604 and 1029 cm^{-1} are attributed to the NH_2 scissors and wagging vibrations, respectively [37], and the absorption band at 1086 cm^{-1} can be assigned to the C–N stretching vibrations [38]. The band at 2965 cm^{-1} is attributed to CH_3 asymmetric vibrations. The bands at 2918 , 2853 and 1385 cm^{-1} correspond to asymmetric and symmetric stretching as well as wagging modes of CH_2 , respectively [35]. The band at 2358 cm^{-1} is attributed to CO_2 in air. The IR spectrum suggests that BA may adsorb on the surfaces of the as-obtained ZnO hexagonal nanodisks.

In the solvothermal reaction system, BA reacted with Zn^{2+} to form $[\text{Zn}(\text{C}_4\text{H}_9\text{NH}_2)_4]^{2+}$, $\text{C}_4\text{H}_9\text{NH}_2$ reacted with H_2O to $\text{C}_4\text{H}_9\text{NH}_3^+$ and OH^- ions, $[\text{Zn}(\text{C}_4\text{H}_9\text{NH}_2)_4]^{2+}$ reacted with OH^- to $[\text{Zn}(\text{C}_4\text{H}_9\text{NH}_2)_4](\text{OH})_2$ [39,40]. Solid ZnO nuclei are formed by the dehydration of the hydroxyl species. The ZnO nanocrystals can continue to grow by the condensation of the surface hydroxyl groups with the zinc-hydroxyl complexes. The chemical reactions to form ZnO are formulated as follows:



As we know, the structure of ZnO can be simply described as a number of alternating planes composed of tetrahedrally coordinated O^{2-} and Zn^{2+} ions, stacked alternately along the c -axis [4], as shown in Fig. 6a. ZnO is a polar crystal with the hexagonal structure, and has a positive polar (001) plane, a negative polar $(00\bar{1})$ plane, and a nonpolar $\{010\}$ plane [4]. In general, the growth velocity under solution conditions is $V_{(001)} > V_{\{010\}} > V_{(00\bar{1})}$ [41], thus one-dimensional (1D) nanorods and nanowires with the crystal elongated along the c -axis have the most common ZnO morphology [42]. However, the growth velocity order among the ZnO facets can be adjusted by passivating the specific ZnO facets using surfactants or polymers. The structure of (001) surface obtained from DFT calculations is shown in Fig. 6b. Obviously, each Zn atom on the (001) face is three-coordinated Zn. However, Zn atom on the $\{010\}$ prismatic faces is two-coordinated Zn [42,43]. So, it is believed that BA may serve as a ligand to Zn and adsorbs selectively on (001) prismatic face of the ZnO nanocrystals in the solvothermal system. The most likely structure is described in Fig. 6c, the presence of BA impede the growth of (001) surface. On the basis of the investigations described above, a possible mechanism was proposed to explain evolution of ZnO nanocrystals with different shapes with the molar ratio of BA to Zn(II). As illustrated in Fig. 7a, when the molar ratio of BA to Zn(II) is 5/1.1, the concentration of BA is lower, there may be a concentration gradient of BA between centre and side of the (001) surface, a step edge is created on the (001) surface, and thus the cone-shaped ZnO nanocrystals are obtained [40]. When the molar ratio of BA to Zn(II) increases to 10/1.1, the

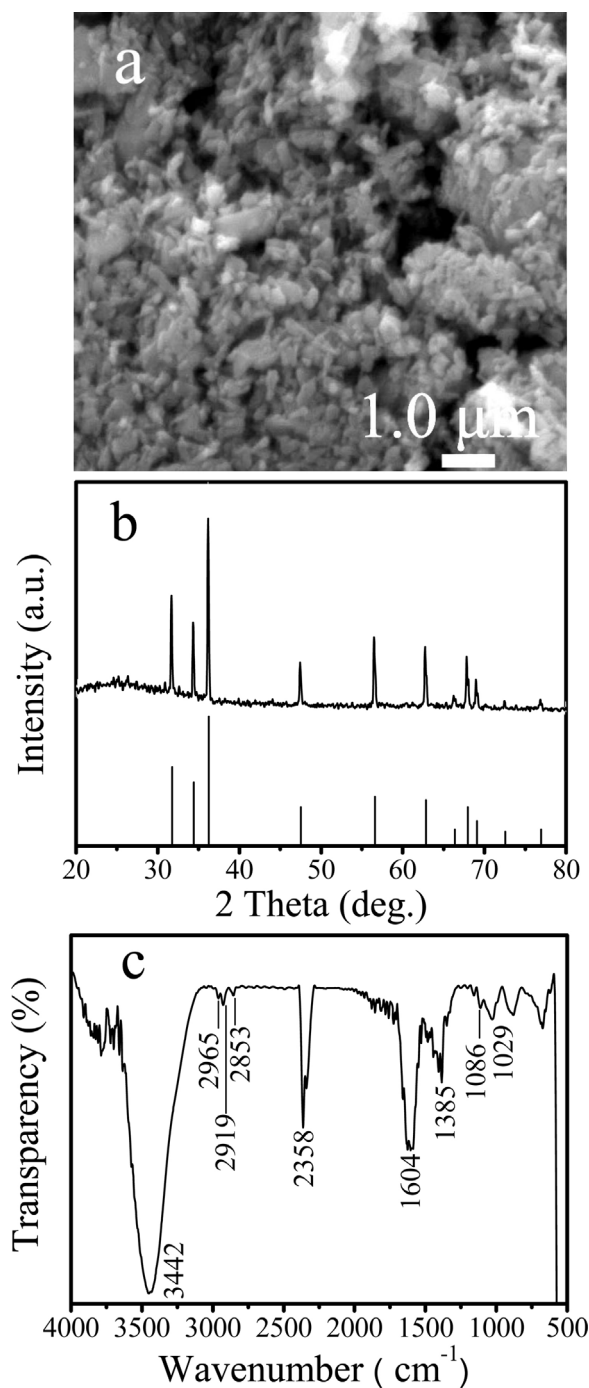


Fig. 5. (a) SEM image and (b) XRD pattern of the products prepared in the zinc acetate-THF solvothermal system without BA at 140 °C for 12 h. (c) IR spectrum of the ZnO nanodisks (sample 3).

concentration gradient of BA weakened due to increasing of BA concentration, and thus platform-shaped ZnO structures are obtained. As the molar ratio of BA to Zn(II) increases to 15/1.1 or 45/1.1, the concentration gradient of BA disappeared, large numbers of BA molecules adsorb selectively on the (001) prismatic faces, limit the growth of (001) surface, and thus the ZnO disk like structures are formed. The thickness of ZnO disk like structures decreases with increasing the molar ratio of BA to Zn(II). The schematic diagram of BA saturated ZnO nanodisk is shown in Fig. 7b.

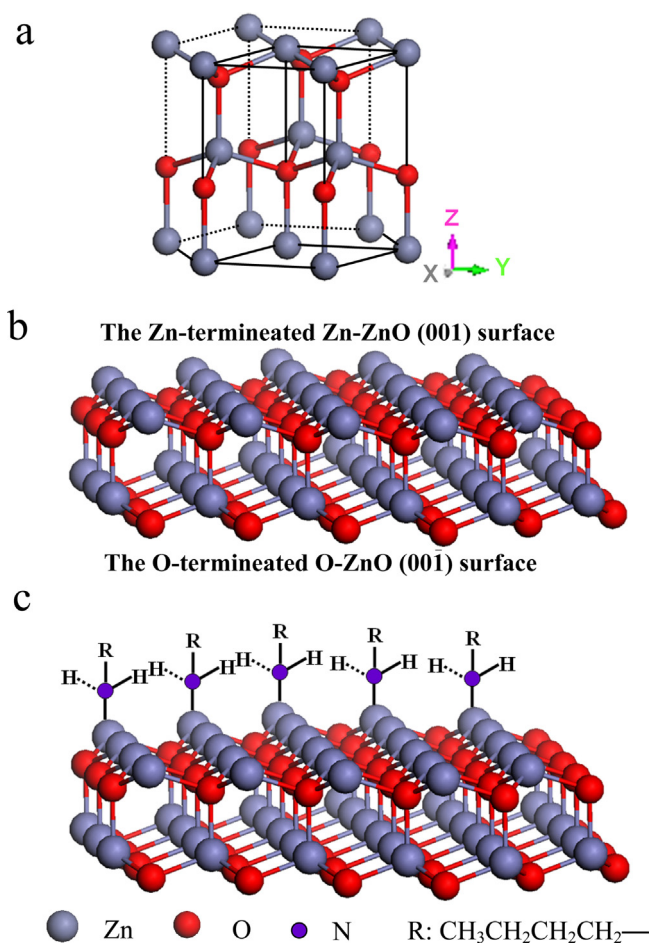


Fig. 6. (a) Crystal structure of wurtzite ZnO. (b) Structure of the exposed ZnO (001) facets. (c) The structure of the BA adsorbed selectively on the (001) prismatic faces.

3.3. Photocatalytic property

To demonstrate the potential applicability in photocatalysis of the as-obtained ZnO nanocrystals with different shapes, we investigated their photocatalytic activity by choosing photocatalytic degradation of MO as a reference. Before evaluation of the photocatalytic activity, adsorption capacity of the as-prepared ZnO samples for MO was studied. Fig. 8a shows the kinetics of MO adsorption on the samples 1, 2, 3 and 4. The C_0 and C represent the concentration of MO at initial and any time, respectively. For samples 1, 2, 3 and 4, after 10 min, the value of C/C_0 is 0.99, 0.98, 0.97 and 0.97, respectively and hardly decreased with an increase on the time, indicating an adsorption/desorption equilibrium between the dye and the ZnO photocatalysts is achieved within 10 min. Therefore, the suspension containing the dye and the catalysts was stirred for 10 min in the dark before the Hg lamp irradiation to establish an adsorption/desorption equilibrium between the dye and the photocatalyst. Fig. 8b

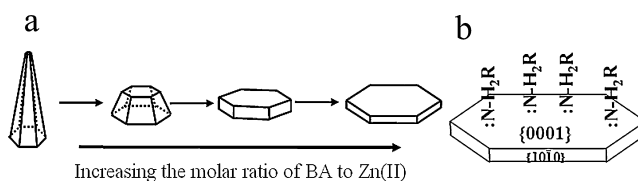


Fig. 7. (a) Schematic illustration of the evolution process of ZnO nanocrystal shapes with increasing of the molar ratio of BA to Zn(II). (b) The schematic diagram of the BA saturated ZnO nanodisks.

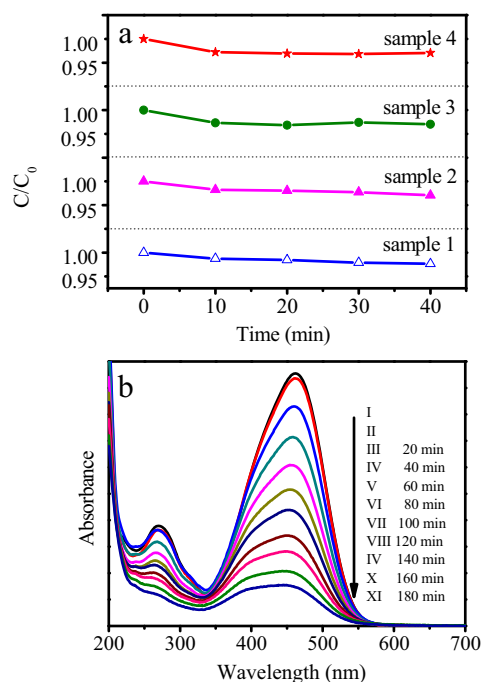


Fig. 8. (a) Adsorption kinetics of MO on samples 1, 2, 3 and 4. (b) Absorption spectra of (I) MO stock solution, (II) MO solution after 10 min adsorption by the sample 3 and (III–XI) MO solution during the photocatalytic degradation process over sample 3.

shows temporal absorption spectra of MO solution during the photocatalytic degradation over the ZnO nanodisks (sample 3). MO shows a maximum absorption band at 462 nm. In the presence of sample 3, the absorption peaks diminished gradually as the irradiation time was extended. The absorption intensity is reduced by about 85% after Hg light irradiation

for 180 min, which implies the destruction of the dye chromogen. Since no new absorption peak was observed, MO may be decomposed. The results implied that the as-synthesized ZnO nanodisks are effective photocatalysts for the degradation of MO.

In addition, we selected the characteristic absorption of MO at 462 nm for monitoring the photocatalytic degradation process over the as-synthesized ZnO nanocrystals with various shapes and (002) orientations (samples 1, 2, 3 and 4) and Degussa TiO₂ P25. Fig. 9a shows the decomposition of MO in solution without catalyst and over samples 1, 2, 3 and 4 as well as P25 under Hg light irradiation as a function of time. As the irradiation time increases, the MO decomposition hardly progress without catalyst under Hg light irradiation. However, the MO decomposition over the as-obtained ZnO nanocrystals with different shapes progresses fleetly, and the MO decomposition rate over sample 4 is faster than that over samples 1, 2 and 3, but is slower than that over P25. The fittings of $\ln(C_0/C)$ plot vs time over P25 and samples 1, 2, 3 and 4 are shown in Fig. 9b. The photodegradations of MO catalyzed by the five kinds of catalysts fit pseudo first-order reaction. i.e. $\ln(C_0/C) = Kt$, K is the apparent rate constant of the degradation. In our experiment, the K value is found to be 0.0376 ± 0.0022 , 0.0256 ± 0.0008 , 0.0109 ± 0.0004 , 0.0093 ± 0.0003 and $0.0071 \pm 0.0002 \text{ min}^{-1}$, over P25 and samples 4, 3, 2 and 1, respectively. The photocatalytic activity of sample 4 is higher than that of samples 3, 2 and 1, but is lower than that of P25. The results indicated that the photocatalytic activity of the as-synthesized ZnO nanocrystals depends on their shapes and $TC_{(002)}$.

It is generally accepted that the catalytic process is mainly related to the adsorption and desorption of molecules on the surface of the catalyst. The BET surface area of Degussa P25 and samples 1, 2, 3 and 4 was measured to be 50.07, 2.62, 2.68, 2.74 and $2.25 \text{ m}^2 \text{ g}^{-1}$, respectively. The apparent rate constant of the degradation per unit surface area of the five kinds of catalysts, as for the basis for the comparison, is examined in this work. The normalized rate constant values (k') of samples 1, 2, 3 and 4 are higher than that

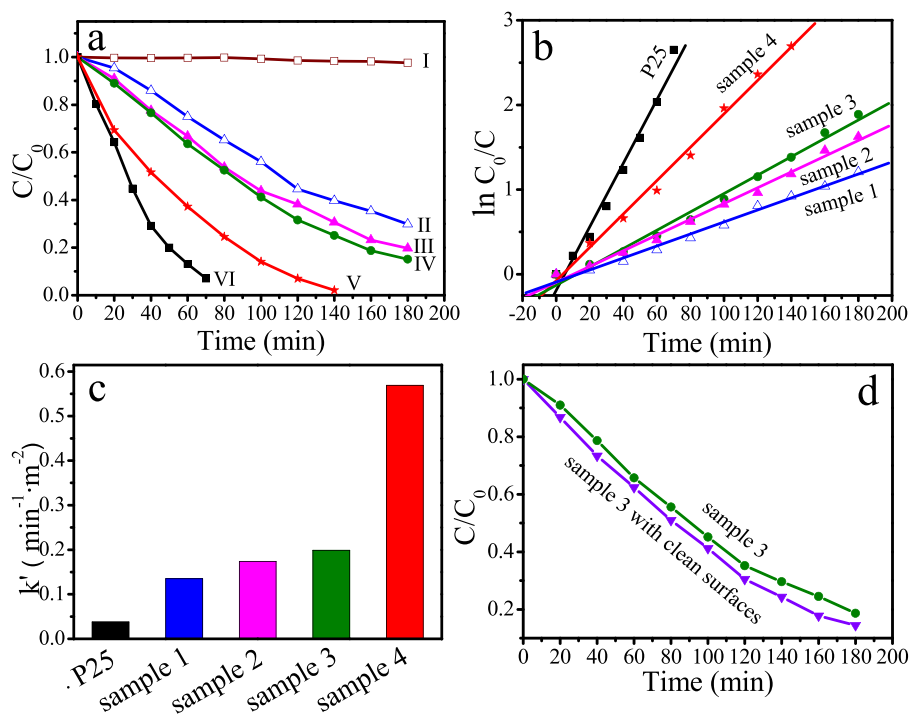


Fig. 9. (a) Photodegradation of the MO solutions without catalyst (I), over samples 1(II), 2 (III), 3 (IV) and 4 (V) as well as Degussa P25 (VI) under Hg light irradiation. (b) The fittings of $\ln(C_0/C)$ plot vs. time over P25 and samples 1, 2, 3 and 4. (c) Normalized apparent rate constant of the degradation per unit surface area (k') over Degussa P25 and samples 1, 2, 3 and 4. (d) Photodegradation of the MO solutions over sample 3 and sample 3 with clean surfaces under UV light irradiation.

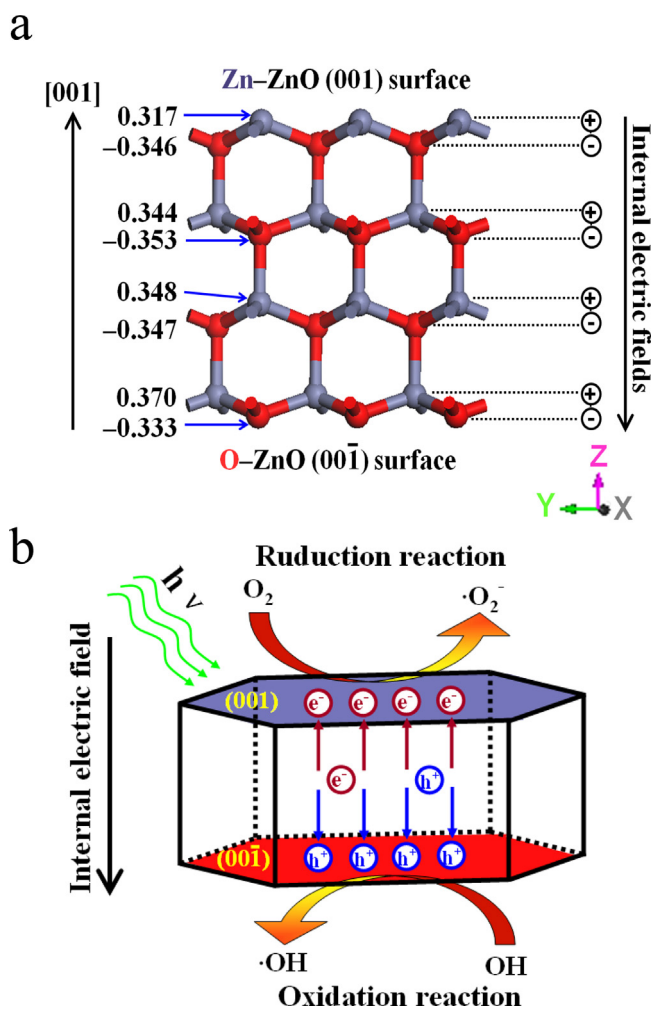


Fig. 10. (a) Atomic charge of $\{001\}$ facets obtained by DFT calculations. (b) The schematic illustration of charge separation between $\{001\}$ polar surfaces and photocatalytic reactions.

of Degussa P25 TiO_2 , as seen in Fig. 9c. The results clearly demonstrate that the as-prepared ZnO nanocrystals with different shapes possess higher intrinsic photocatalytic activity than Degussa P25 TiO_2 , and the photocatalytic activity is enhanced with increasing value of $\text{TC}_{(002)}$ and percentage of $\{001\}$ surfaces. In addition, the sample 3 was dried in a vacuum oven at 60°C for 3 days to remove the BA molecules adsorbed on the (001) surface further. The photocatalytic activity of the sample 3 with clean surfaces was investigated, and the result is shown in Fig. 9d. It was found that the MO decomposition rate over the sample 3 with clean surfaces is faster than that over sample 3. It is reasonable to conclude that the exposed $\{001\}$ facets are highly reactive facets for degradation of MO.

3.4. Charge separation between polar ZnO $\{001\}$ surfaces and photocatalysis mechanism

As we know, the overall photocatalytic reaction involves three major steps: (i) absorption of light by semiconductor to generate electron hole pairs, (ii) charge separation and migration to the surface of semiconductor and (iii) generation of active species and pollutant degradation [44,45]. The photocatalytic activity is cooperatively determined by the electronic structure and surface properties of photocatalysts. The exposed $\{001\}$ facets are polar surfaces, they consist of a positive the Zn-terminated Zn-ZnO

surface or Zn-ZnO (001) and a negative the O-terminated O-ZnO surface or O-ZnO (00 $\bar{1}$), as shown in Fig. 6b. Atomic charge distribution of $\{001\}$ facet obtained from periodic DFT calculations is shown in Fig. 10a. Apparently, each layer contains all positive Zn^{2+} ions or all negative O^{2-} ions in the [001] direction. Zn atomic charge on the Zn-ZnO (001) plane is +0.317 and O atomic charge on the O-ZnO (00 $\bar{1}$) plane is -0.333. An internal electric field thus is generated between Zn-ZnO (001) and O-ZnO (00 $\bar{1}$) planes due to the spontaneous polarization. When the ZnO nanosheets with exposed $\{001\}$ polar faces were employ as photocatalysts, photogenerated electrons and holes migrate to positive polar Zn-ZnO (001) planes and negative polar O-ZnO (00 $\bar{1}$) planes, respectively, under the internal electric field (Fig. 10b). The reduction and oxidation reactions take place on the positive Zn-ZnO and negative O-ZnO planes, respectively (Fig. 10b). The good charge separation between polar $\{001\}$ surfaces can effectively reduce the probability of recombination of photogenerated electrons and holes, and thus the polar $\{001\}$ facets are highly reactive facets for degradation of MO.

4. Conclusions

In summary, controlled synthesis of ZnO nanocrystals with various (002) orientations have been achieved by changing the molar ratio of BA to Zn(II) in the zinc acetate-BA-THF solvothermal system. The role of BA in the formation of the ZnO nanocrystals with various (002) orientations and shapes was investigated, and a possible mechanism was proposed. This simple, mild solution approach to fabricate ZnO nanocrystals with controllable (002) orientations can be easily scaled up and potentially extended to the synthesis of other wurtzite II–VI semiconductor nanocrystals. The polar $\{001\}$ facets were found to be highly reactive facets for degradation of MO. Based on the polar structure of the exposed $\{001\}$ surfaces, a charge separation model between polar $\{001\}$ surfaces was proposed. The charge separation model may be applied to other semiconductor nanocrystal with highly photocatalytic activities. Our results demonstrate that it is feasible to increase photocatalytic properties of semiconductor-based photocatalysts with the hexagonal structure by selectively exposing the $\{001\}$ polar facets. The present study inspired us to design and fabricate more effective photocatalysts and new type photoelectrodes, solar cells or photoelectric devices.

Acknowledgements

This work was supported by the National Natural Science Foundation of China (Grant No. 21073116), the Natural Science Foundation of Shaanxi Province (Grant No. 2010JM2011) and the Fundamental Research Funds for the Central Universities (Grant GK201101004 and GK201402019).

References

- [1] H. Tong, S.X. Ouyang, Y.P. Bi, N. Umezawa, M. Oshikiri, J.H. Ye, *Adv. Mater.* 24 (2012) 229–251.
- [2] Z.Y. Jiang, Q. Kuang, Z.X. Xie, L.S. Zheng, *Adv. Funct. Mater.* 20 (2010) 3634–3645.
- [3] K.B. Zhou, Y.D. Li, *Angew. Chem. Int. Ed.* 51 (2012) 602–613.
- [4] Z.L. Wang, *J. Phys. Condens. Matter* 16 (2004) R829–R858.
- [5] M.H. Huang, S. Mao, H. Feick, H.Q. Yan, Y.Y. Wu, H. Kind, E. Weber, R. Russo, P.D. Yang, *Science* 292 (2001) 1897–1899.
- [6] Z.Y. Fan, J.G. Lu, *Appl. Phys. Lett.* 86 (2005) 032111.
- [7] H. Kind, H.Q. Yan, B. Messer, M. Law, P.D. Yang, *Adv. Mater.* 14 (2002) 158–160.
- [8] C.H. Wang, X.F. Chu, M.M. Wu, *Sens. Actu. B* 113 (2006) 320–323.
- [9] M. Law, L.E. Greene, J.C. Johnson, R. Saykally, P. Yang, *Nat. Mater.* 4 (2005) 455–459.
- [10] Z.L. Wang, J.H. Song, *Science* 312 (2006) 242–245.
- [11] D. Li, H. Haneda, *Chemosphere* 51 (2003) 129–137.
- [12] E.S. Jang, J.H. Won, S.J. Hwang, J.H. Choy, *Adv. Mater.* 18 (2006) 3309–3312.

- [13] L.N. Zhang, H.Q. Yang, J.H. Ma, L. Li, X.W. Wang, L.H. Zhang, S. Tian, X.Y. Wang, *Appl. Phys. A* 100 (2010) 1061–1067.
- [14] M.Y. Guo, A.M.C. Ng, F.Z. Liu, A.B. Djurišić, W.K. Chan, H.M. Su, K.S. Wong, *J. Phys. Chem. C* 115 (2011) 11095–11101.
- [15] Y.X. Wang, X.Y. Li, G. Lu, X. Quan, G.H. Chen, *J. Phys. Chem. C* 112 (2008) 7332–7336.
- [16] X.J. Wang, Q.L. Zhang, Q. Wan, G.Z. Dai, C.J. Zhou, B.S. Zou, *J. Phys. Chem. C* 115 (2011) 2769–2775.
- [17] D.W. Chu, Y. Masuda, T. Ohji, K. Kato, *Langmuir* 26 (2010) 2811–2815.
- [18] T.J. Sun, J.S. Qiu, C.H. Liang, *J. Phys. Chem. C* 112 (2008) 715–721.
- [19] J.H. Zeng, B.B. Jin, Y.F. Wang, *Chem. Phys. Lett.* 472 (2009) 90–95.
- [20] C.H. Ye, Y. Bando, G.Z. Shen, D. Golberg, *J. Phys. Chem. B* 110 (2006) 15146–15151.
- [21] F. Lu, W.P. Cai, Y.G. Zhang, *Adv. Funct. Mater.* 18 (2008) 1047–1056.
- [22] M. Wang, G.T. Fei, L.D. Zhang, *Nanoscale Res. Lett.* 5 (2010) 1800–1803.
- [23] A.H. Lei, B.H. Qu, W.C. Zhou, Y.G. Wang, Q.L. Zhang, B.S. Zou, *Mater. Lett.* 66 (2012) 72–75.
- [24] Y.Q. Yang, G.H. Du, X. Xin, B.S. Xu, *Appl. Phys. A* 104 (2011) 1229–1235.
- [25] B.X. Li, Y.F. Wang, *J. Phys. Chem. C* 114 (2010) 890–896.
- [26] Y.L. Ying, T. Song, H.W. Huang, X.S. Peng, *Appl. Phys. A* 110 (2013) 351–359.
- [27] G.K. Zhang, X. Shen, Y.Q. Yang, *J. Phys. Chem. C* 115 (2011) 7145–7152.
- [28] H.G. Yang, G. Liu, S.Z. Qiao, C.H. Sun, Y.G. Jin, S.C. Smith, J. Zou, H.M. Cheng, G.Q. Lu, *J. Am. Chem. Soc.* 131 (2009) 4078–4083.
- [29] C.X. Li, L.J. Han, R.J. Liu, H.H. Li, S.J. Zhang, G.J. Zhang, *J. Mater. Chem.* 22 (2012) 23815–23820.
- [30] R. Jin, M.Y. Su, J. Wang, P. Zhang, M. Cui, Y. Chen, H.Q. Yang, *Mater. Res. Bull.* 47 (2012) 3070–3077.
- [31] Z.K. Zheng, B.B. Huang, Z.Y. Wang, M. Guo, X.Y. Qin, X.Y. Zhang, P. Wang, Y. Dai, *J. Phys. Chem. C* 113 (2009) 14448–14453.
- [32] B. Delley, *J. Chem. Phys.* 92 (1990) 508–517.
- [33] J.P. Perdew, K. Burke, M. Ernzerhof, *Phys. Rev. Lett.* 77 (1996) 3865–3868.
- [34] F.L. Hirshfeld, *Theoret. Chim. Acta* 44 (1977) 129–138.
- [35] H. Zhao, W.Y. Yin, M.Y. Zhao, Y.Z. Song, H.Q. Yang, *Appl. Catal. B: Environ.* 130–131 (2013) 178–186.
- [36] L.H. Zhang, H.Q. Yang, J. Yu, F.H. Shao, L. Li, F.H. Zhang, H. Zhao, *J. Phys. Chem. C* 113 (2009) 5434–5443.
- [37] T. Morimoto, J. Imai, M. Nagao, *J. Phys. Chem.* 78 (1974) 704–708.
- [38] C.T. Chiang, J.T. Roberts, *Chem. Mater.* 23 (2011) 5237–5242.
- [39] H.Q. Yang, Y.Z. Song, L. Li, J.H. Ma, D.C. Chen, S.L. Mai, H. Zhao, *Cryst. Growth Des.* 8 (2008) 1039–1043.
- [40] J.H. Ma, H.Q. Yang, Y.Z. Song, L. Li, X.L. Xie, R.N. Liu, L.F. Wang, *Sci. China, Ser. E* 52 (2009) 1264–1272.
- [41] R.A. Laudise, A.A. Ballman, *J. Phys. Chem.* 64 (1960) 688–691.
- [42] L. Li, H.Q. Yang, J. Yu, Y. Chen, J.H. Ma, J.Y. Zhang, Y.Z. Song, F. Gao, *J. Cryst. Growth* 311 (2009) 4199–4206.
- [43] C. Wöll, *Prog. Surf. Sci.* 82 (2007) 55–120.
- [44] J.H. Yang, D.G. Wang, H.X. Han, C. Li, *Acc. Chem. Res.* 46 (2013) 1900–1909.
- [45] J. Jiang, K. Zhao, X.Y. Xiao, L.Z. Zhang, *J. Am. Chem. Soc.* 134 (2012) 4473–4476.